A STUDY OF THE STRUCTURE OF THE T-LAYER OF BACILLUS BREVIS

U. Aebi, P. R. Smith, J. Dubochet, Carol Henry,* and E. Kellenberger

Biozentrum der Universität Basel, Klingelbergstrasse 70, CH–4056 Basel, Switzerland

INTRODUCTION

General Introduction

A study of *Bacillus brevis* by McNary, Brinton, and Carnahan (1) showed that it possesses an external, regularly arranged protein layer which could be seen on electron micrographs of shadowed or negatively stained intact cells. This so-called T-layer could be removed and then purified as described by Henry (2). Further experiments (2) showed that low pH treatment caused the layer to dissociate reversibly into smaller parts and that treatment of the intact layer with proteolytic enzymes (e.g., pronase) led to the formation of tetragonally arranged cylindrical structures. SDS gel electrophoresis of planar and cylindrical T-layer indicated that the molecular weight of the major protein component passed from 140,000 to 125,000 daltons, respectively.

In this paper we present the results of an analysis of electron micrographs of negatively stained native and pronase-treated T-layers using both the well-known methods of optical diffraction and filtration (3–9) and the digital computer Fourier transform (10) and filtration method. We had two aims: first to establish the two-dimensional structure and arrangement of the protomer in the tetragonal net (2) to the best available resolution, and second to make a qualitative comparison between the optical and digital methods using the cylindrical T-layer structure as an example. Until now the use of digital methods in the study of planar or flattened cylindrical lattices has been fairly limited (11). Computer reconstructions have been used extensively in the analysis of helical and spherical structures, however (12, 13).

Mathematical details and some remarks concerning filtration techniques can be found in the appendix where we also discuss the relation between the filtration method using Fourier transforms and Markham's method of linear superposition (14).

*Present address: Princeton University, Department of Biology, Princeton, New Jersey 08540

Optical and Computer Filtration

The optical and computer methods for filtering Fourier transforms differ in two important respects. First of all the mathematical quantity transformed in the two systems is different. In the optical system one transforms the transmissivity of the film, whereas in the computer one deals directly with its optical density.* This difference is important in principle because, to a first approximation, the optical density of the micrograph (OD) is linearly related to the mass thickness of the specimen (15). Consequently a super-position of two plane layers will give rise to a micrograph whose optical density is, in this approximation, linearly related to a sum of contributions from each of the layers. The transmissivity of the micrograph, however, is related to the product of the contribution from the two layers. This fact is reflected in the Fourier transform obtained by the optical system where diffraction spots can sometimes be seen due to the convolution of the periodic information from the two lattices (9). Provided these extra spots do not coincide with the principal maxima they do not cause any trouble in a practical filtration (6) because the separation of the two layers can be achieved to a good approximation due to the dominance of the zero order.

The second difference is the most important and concerns the fact that the digital transform is necessarily a discrete transform of a function sampled on a regular sampling lattice. The Fourier transform is also sampled, but on a lattice whose spacing is the reciprocal of the overall window size. This means that a wave in the real space picture whose spatial frequency does not correspond exactly to one of the transform sampling points cannot be represented by only one nonzero number in the sampled transform. If such a spatial frequency is necessary for the reconstruction it is not possible to construct a simple "mask" for the computer transform which will transmit this frequency alone. Consequently, in our work we manipulated the sampling grid in real space so that the spatial frequencies we wished to transmit through our computer mask lay as close as possible to Fourier space sampling points. In the case of the optical analogue transform all spatial frequencies up to a certain limit can be sampled because the optical Fourier transform is continuous. Consequently, the quality of filtering procedure mainly depends on the skill of the person constructing the filter masks.

Notwithstanding what has been said, useful results may be obtained from the computer even when the important spatial frequencies do not lie exactly on the sample points, by simply constructing a mask which transmits all frequencies close to the one of interest. This leads to an improvement in the visible structure and is helpful as a first step in the analysis when searching for the alignment and scaling of the lattice vectors, but the signal-to-noise ratio of the overall picture is, however, smaller than that obtained with the other method because of the extra points which have been transmitted through the computer filter mask. This is clearly not the optimum information processing situation.

MATERIALS AND METHODS

Preparation of T-Layer Samples

Removal and subsequent purification of T-layer sheets from intact *B. brevis* cells

---

*In fact, due to the finite size of the densitometer spot, the quantity measured is the integral of the transparency over the film area illuminated by the densitometer spot.

was achieved by following the method described by Henry (2). Intact cells suspended in sterile water were broken by sonication and then centrifuged for 5 min at 1085 g. The super-natant which contained the cell wall fragments was then washed 5 times by centrifugation (12,000 g for 10 min) and the final pellet was resuspended in sterile water to give a con-centration of 0.1 gm cell wall/ml H_2O. To detach the T-layers from the cell wall fragments, an equal volume of 2 M guanidine hydrochloride was added and the mixture was stirred gently for 2.5 hr.

This solution was then layered onto a sucrose step gradient, consisting of 15 ml of 15% sucrose buffered with tris HCl, pH 7.5, layered over 15 ml of 40% sucrose, and centrifuged for 30 min at 900 g. The bands containing the T-layer fractions were centri-fuged for 30 min at 23,000 g and the pellets resuspended in 0.1 M KCl. By subsequently adding sodium pyrophosphate the pH was lowered to 2.5 in order to dissociate the T-layers. These low pH fractions were centrifuged for 30 min at 23,500 g and the supernatants were neutralized up to pH 6.5 to give reassembled planar T-layer sheets. To get the cylindrical modification, the T-layer sheets were treated with 0.5% pronase for 60 min (B grade, Calbiochemical). Both samples were then preserved by adding 1% sodium azide and were stored in the cold.

Electron Microscopy

Samples of T-layers intended for examination in the electron microscope were first fixed with 1% formaldehyde and then adsorbed to carbon supporting films which were rendered hydrophilic by glow discharge in air at low pressure and finally stained with 2% sodium phosphotungstate at pH 7. These preparations were examined in minimum beam exposure, using the beam rocking method of Williams and Fisher (16), in a Philips E.M. 301 at magnifications in the range of 35,000 to 40,000. The vacuum conditions of the micro-scope were such that the contamination rate at crossover was a few angstroms per minute. Micrographs were recorded on 70mm Kodalith LR 2572 film and developed in Kodak DK 60a developer. Calibration of the microscope magnification was performed by measuring grating replicas of known spacings (607 Polaron, carbon grating replica, crossed lines, 54,800 lines/inch) which were checked in an optical microscope. Care was also taken to avoid errors due to lens hysteresis and the variable height of the specimen plane in the microscope; the latter was checked by monitoring the objective lens current. As a result the relative magnifications between successive pictures were estimated to be stable to within ± 1%. The absolute accuracy of the magnification of the microscope was estimated to be of the order of ± 3%.

The instrumental resolution was checked and was always found to be better than 3.4 Å (line resolution) on graphite. Taking this resolution check into account together with the instrument and photographic film properties, we were able to record micrographs with a resolution of at least 10 Å at a magnification of 35,000.

Micrographs of T-layers which produced diffraction patterns with strong high-order spots and which showed relatively fine detail and a large gray level range on direct inspec-tion were selected for subsequent processing.

Processing Micrograph Data

The optical method. Optical diffraction patterns and reconstructions were done on a 3-times folded diffractometer designed by Boy de la Tour, Bron, and Kellenberger (Fig. 1). The light source was a 1 mW He– Ne laser (Spectra Physics, model 132) and the

transformation lens had a focal length of 1185 mm which resulted in a diffractometer constant of

$$h_c = \lambda \cdot f = 0.75$$

The micrograph was illuminated with a parallel light bundle of almost equal intensity over a radius of about 1 cm.

As reconstruction lens a high-quality objective (Schneider Repro-Claron 1:9) with a focal length of 610 mm was used. It was positioned behind the filter plane at a distance such that a 1:1 magnification of the filtered pictures was obtained.

In order to avoid damage to the original micrographs contact prints were used. These were recorded on Rototype FRK film (Typon) and developed so as to obtain a gamma of 1 inside the gray level range of the micrographs. This was checked by reproducing a calibrated step wedge under the same conditions and measuring the reproduced step wedge on a Joyce Loebl Chromoscan. Diffraction patterns and reconstructions were recorded on Ilford FP4 film.
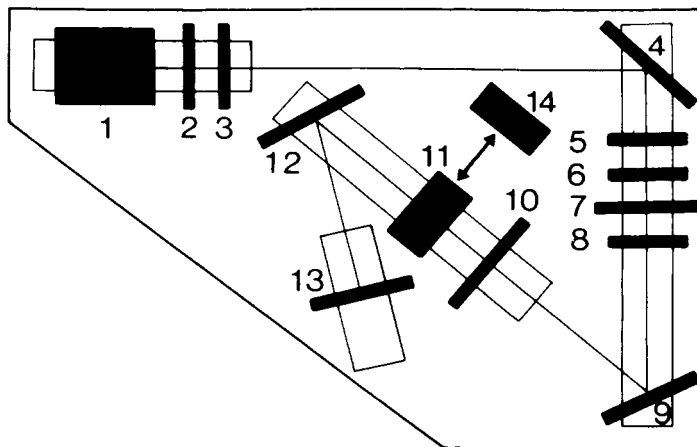

```
 1 : He-Ne-light source
 2 : Lens, f = 50 mm, Ø = 16 mm )
 3 : pinhole, Ø = 100 µm          )  beam expanding system
 4 : Plane mirror
 5 : Lens, f = 1185 mm, Ø = 71 mm; d(3,5) = 1185 mm; with
     concentric circular aperture of Ø = 2o mm
 6 : Variable rectancular aperture for framing the micro-
     graphs
 7 : Object plane, stage for mounting the micrographs
 8 : Lens, f = 1185 mm, Ø = 71 mm
 9 : Plane mirror
10 : Diffraction plane, stage for recording diffraction
     patterns or mounting filter masks
11 : Reconstruction lens, f = 610 mm, Ø = 68 mm
12 : plane mirror
13 : Reconstruction plane, stage for recording recon-
     structions
14 : Microscope for observing diffraction patterns or
     reconstructions, 10x magnification
```

Fig. 1. Design of the folded diffractometer.

Fourier transforms and reconstructions were made of square (1 cm × 1 cm) windows from the best preserved parts of the micrographs so that an area of 400 to 500 unit cells was obtained when a standard electron microscope magnification of 35,000 to 37,000 had been used.

The filtration masks were made following the procedure described by Leonard et al. (8) with the exception that 0.1 mm copper foils coated with Kodak thin film resist (KTFR) were used instead of KAR3 coated sheet brass. Errors in mask dimensions and hole positions were kept to less than 1%. The filter holes were always circular and had a diameter of about 1/5 of the reciprocal lattice constant so that we were averaging over about 100 unit cells (see first part, Appendix). As a result the reconstructed unit cells were not exactly identical over the processed window.

Twofold rotational averaging of the reconstructions was performed by superimposing two identical transparent film copies, which were rotated 180° with respect to one another. The optical density of these films was only half the optical density of the ordinary reconstructions so that the superpositions had the same final optical density. The reconstructions from the diffractometer were enlarged in a two-step process to a final magnification of about 2,500,000.

The computer method. Micrographs of T-layers were enlarged so that the lattice constant of the T-layer as seen in the enlargement was 1.2 mm, and were recorded on Rototype FRK film (Typon). This film was cut so that it could be scanned parallel to one lattice vector by the densitometer (Optronics Photoscan model P–1000). Measurements of the optical density of the film were collected from a selected area of the film on a 50 μm raster, written directly onto magnetic tape and transferred to an IBM 370/155 computer. These data were then preprocessed to recover the original micrograph optical density, using data obtained from a calibrated step wedge enlarged under the same conditions as the micrograph and measured on a Joyce Loebl Chromoscan.

A region of roughly 10 × 10 unit cells was selected and digitally Fourier transformed. This was then reverse transformed using an area of 3 × 3 transform sample points around each of the expected reciprocal lattice points. The result was a less noisy picture on which the lattice parameters could be measured directly. The sampled data were then transferred using a bilinear interpolation scheme (see second part, Appendix) from the original sampling grid to a new grid chosen so that the sampling raster vectors were aligned with and scaled to the lattice vectors previously determined giving exactly 24 × 24 sample points per unit cell. In order to check the choice of vectors which had been made, computational searches were done varying skew angles and lattice constants to find the parameters which maximized the total image power in the reciprocal lattice. Such a procedure was very expensive in computer time and generally confirmed the results obtained by direct measurement on the picture. It was found that the quality of the final reconstructions and the symmetry residuals also provided a sensitive check on the choice of vectors.

After the transfer of the data to the new grid a region of exactly 10 × 10 unit cells (240 × 240 matrix) was selected and digitally transformed and then reconstructed using only those transform points on the reciprocal lattice of the T-layer, a procedure equivalent to doing a Markham linear superposition with a computer (see first part, Appendix).

Fourfold rotational symmetrizations were done by fourfold averaging of the Fourier transforms and a residual was calculated which gave the percentage of the total image power which had been lost in the averaging step. This residual was not a sensitive test of the degree of symmetry of high-frequency terms because of their relatively small contri-

bution to the total image power but it quickly revealed any asymmetry in the image information or incorrect choice of symmetry center.

Pictorial output was obtained on a line printer using the method described by MacLeod (17). Upper and lower cutoff values were chosen to give the best correspondence with the optical transform pictures.

RESULTS

Statistical Analysis of T-Layer Lattice Parameters

We established the lattice parameters of both the planar and cylindrical forms by statistical analyses of measurements from 50 micrographs of preparations of mixtures of the two forms. At least one of each of the two forms was measured on every micrograph used. The results are tabulated and plotted in Table I and Fig. 2, respectively.

g_1 and g_2 are the lattice vectors, g_1 and g_2 the lattice constants of the cylindrical form. Their arrangement (including the handedness, which was determined and found to be the same on 15 platinum shadowed cylinders) is shown in Fig. 2a. In Fig. 2b we have plotted g_2 against g_1 to illustrate the fact hat g_1 is consistently shorter than g_2 (all the points lie to the left of the line $g_1 = g_2$). In the samples of the planar form we could not distinguish between g_1 and g_2 and so we defined a mean lattice constant g as: g = $(g_1 + g_2)/2$. In order to compare planar and cylindrical forms we used this definition for both cases, as shown in Fig. 2c.

The distribution of the skew angles (skew angle = deviation of the angle between the two lattice vectors from $90°$) of both forms is shown in Fig. 2d. In the case of the cylinders, with a well-defined handedness, the sign of the skew angle is clearly defined. In the planar case it is not possible to tell the difference between positive and negative skews and consequently we assume a mean value of $0°$ for the planar distribution.

In Fig. 2e the distribution of the pitch angle of the cylinders is drawn, where the pitch angle is defined, as shown in Fig. 2a.

Table I summarizes the mean values and the standard deviations of the lattice parameters calculated from the data of the histogrammed distributions. It should be noted that the standard deviations of the lattice constants are relative deviations; that is, they are the result of a systematic series of measurements under reproducible conditions and consequently are valid for a comparison. The absolute values, however, were estimated to be reliable only within $\pm 5\%$, taking into account the uncertainties in the microscope magnification.

TABLE I.

	Planar	Cylinder
g_1	—	130.94 ± 0.71 Å
g_2	—	131.60 ± 0.71 Å
g	131.15 ± 1.15 Å	$131.25 \pm .78$ Å
Pitch	—	$39.0° \pm 0.5°$
Skew	$0° \pm 0.5°$ (?)	$1.0° \pm 0.5°$

Reconstruction of the Cylinder Preparations Using 3 to 5 On—Axis Diffraction Orders

Some consequences of the computer processing. In the Materials and Methods section we have discussed in detail the processing steps involved in obtaining all the reconstructions given in this paper. The computer processing does, however, deserve more comment as the consequences of the transfer of data from one sampling grid to another are not immediately obvious. We pointed out in the Optical and Computer Filtration section of the Introduction that a discrete Fourier transform cannot be efficiently filtered if the spatial frequencies one wishes to preserve are not sampled on the sampling grid. In order
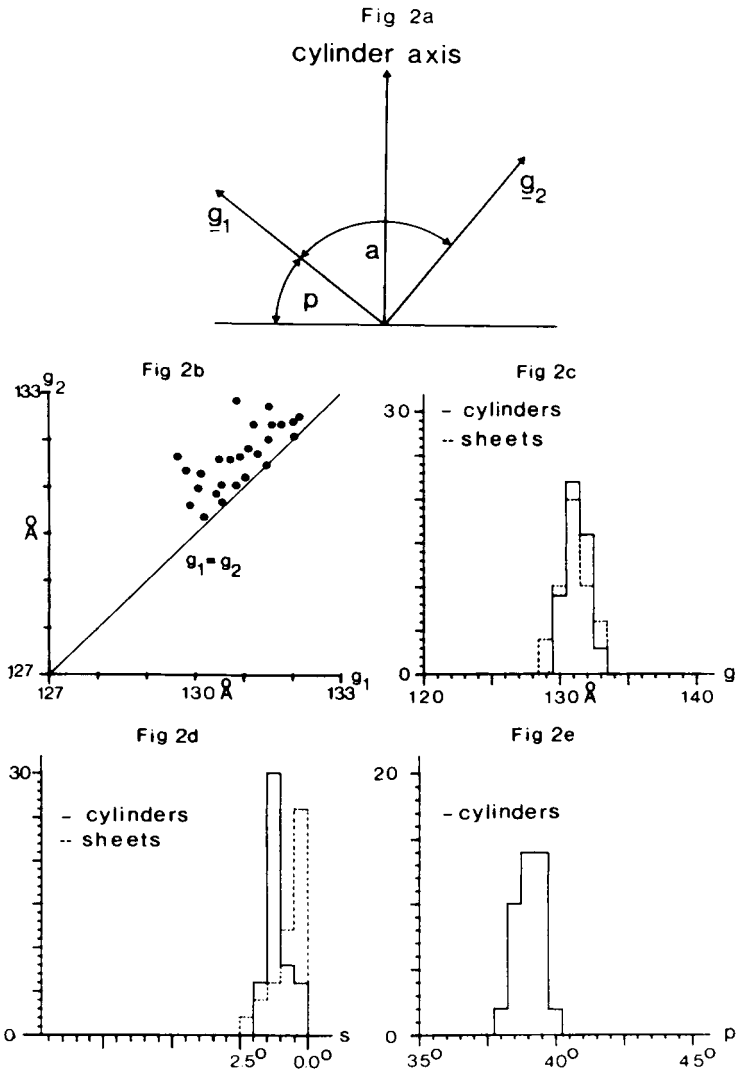
Fig. 2. Statistical analysis of T—layer lattice parameters. (a) Cylindrical lattice parameters. (2) Distribution of cylinder lattice vector lengths. (c) Histogram of cylinder and sheet lattice constants. (d) Histogram of cylinder and sheet lattice skew angles. (e) Histogram of cylinder pitch angles.

to achieve this coincidence between the spatial frequencies and the sample grid the data were transferred using a bilinear interpolation scheme to a skewed sample grid whose lattice lines were parallel to the T-layer lattice (see Materials and Methods and Appendix, second part). This procedure is perfectly satisfactory from a mathematical point of view provided that the new coordinate system is always regarded as a skew system. It is only possible to regard this new system as the "correct" system, in the sense that it has removed a distortion in the original lattice, if the distortion occurred isotropically over the whole unit cell. In the case of a distorted lattice, where the protein subunits of the unit cell had moved in relation to each other while remaining relatively undistorted themselves, the change from one coordinate system to another would introduce a second-order distortion of the subunits as well as "remove" the skew.

In our case, where skew angles were always less than $2°$, shearing artifacts introduced by the coordinate transformation, could be ignorned because they could have contributed errors in mislocation of mass of no more than 1 Å over the width of a single subunit. Because this skew was so small we could treat the coordinate transformation as a correction and rotationally average the unit cells by fourfold symmetrizing their Fourier transforms. This step would almost certainly have been erroneous if the skew angle had been large.

In general one would expect that the minimum energy configuration of a P4 lattice which had been bent into a closed cylinder could easily involve a small skew in the natural state. One could argue that in such cases the skew angle should be reintroduced into the reconstruction. In our case, however, the angle was too small for this to be worthwhile and in any case the true pitch of the reassembled cylinders in solution could not be found.

Reconstructions. Figure 3a shows the initial micrograph; the area used for reconstruction is marked with "A" (the marked areas contain the array of 10 × 10 unit cells we used for the computer reconstructions: for the optical reconstructions we used an area of about 20 × 20 unit cells which included the computer-processed area). The diffraction pattern of this area is presented in Fig. 3b, the left-hand side being the optical diffraction pattern and the right-hand side being the computer-generated one. A comparison between these two is interesting because in the computer diffraction pattern only the diffraction spots for one layer can be seen clearly; the others are, in general, blurred into the background noise because the sampling grid was not aligned with this lattice (see Introduction).

Figures 4a, b show 2 × 2 unit cells of five-order reconstructions of the two superposed layers seen in areas of fig. 3a; Fig. 4c shows a five order reconstruction of the single layer seen in area B. From the handedness of the cylinders, determined on platinum-shadowed samples (see above), we concluded that Figs. 4a, c are reconstructions of the upper layer of the flattened cylinder. All the reconstructions shown in Fig. 4 have been rotationally symmetrized, twofold in the optical case and fourfold in the computer.

In order to study the build-up of information, we made a series of reconstructions using successively 3, 4, and 5 on-axis orders in the filtrations (on-axis means parallel to the reciprocal lattice vectors which are parallel to the sampling grid in Fourier space). An example of such a series is shown in Fig. 5a, b, c using data for the upper layer of the area A in Fig. 3a. It can be seen from these reconstructions that the largest change in the structure comes about when the fourth order is included and the structure finally becomes clear. The inclusion of the fifth order makes little or no difference to the results. All pictures in Fig. 5 are unsymmetrized and so a comparison of Fig. 4a and 5c illustrates the effect of symmetrization. (The "graininess" seen in the optical reconstructions in Fig. 5 is averaged

away by the superpositions needed to produce those in Fig. 4.) We calculated on the computer that less than 5% of the image power was lost on fourfold symmetrization. In Fig. 6 the optical reconstruction of another cylindrical T-layer is presented. Fig. 6a shows the unprocessed micrograph and Fig. 6b shows an enlargement of the area marked "A" in Fig. 6a to the same scale as the reconstruction of 10 × 10 unit cells seen in Fig. 6c.

To obtain an estimate of the noise content in the original micrographs a reconstructed area was subtracted in the computer from the original by using a "negative" filtration; that is, all the information lying on the sample points of the reciprocal lattice of the T-layer (including the "periodic" noise) was filtered out and only the "nonperiodic" noise was reconstructed. The standard deviation from the mean of this noise was then determined to be roughly ± 20% of the total variation in the optical density due to the reconstructed structure over one unit cell.
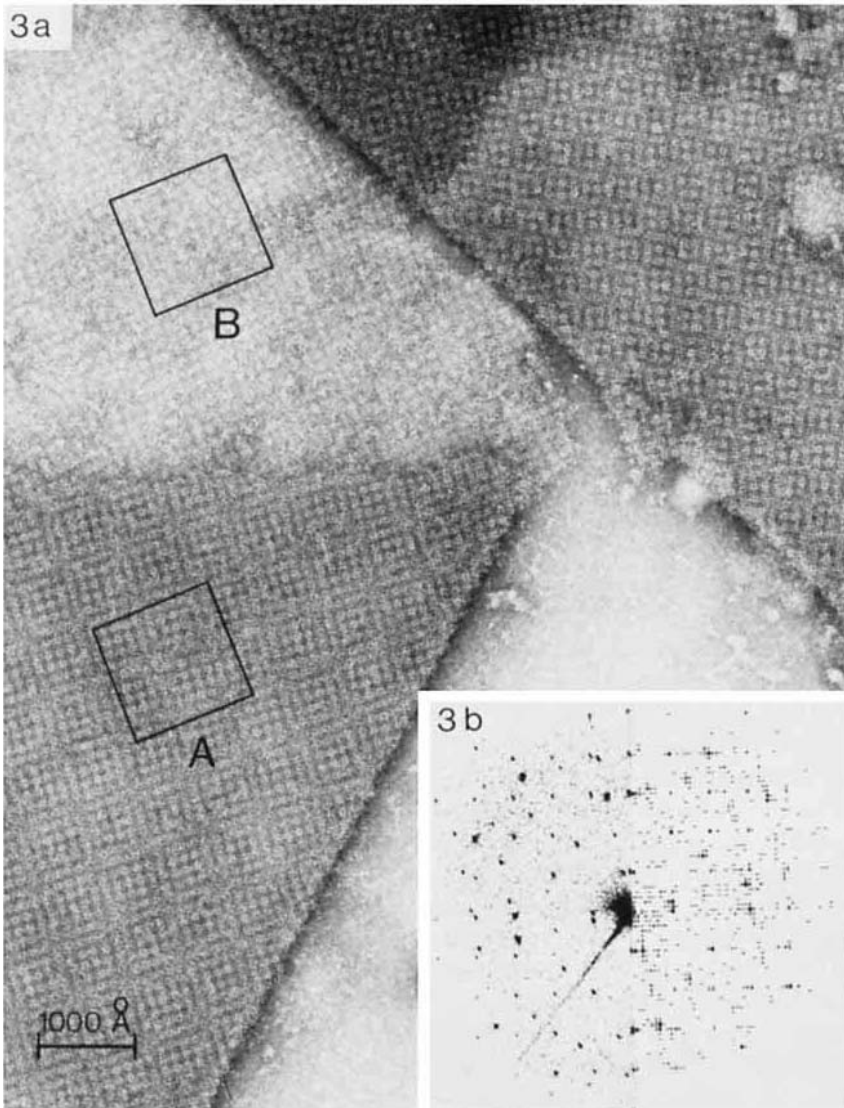
Fig. 3. (a) Micrograph of T–Layer cylinder. (b) Diffraction pattern of area "A" on micrograph. Left-hand side: Optical; right-hand side: computer.
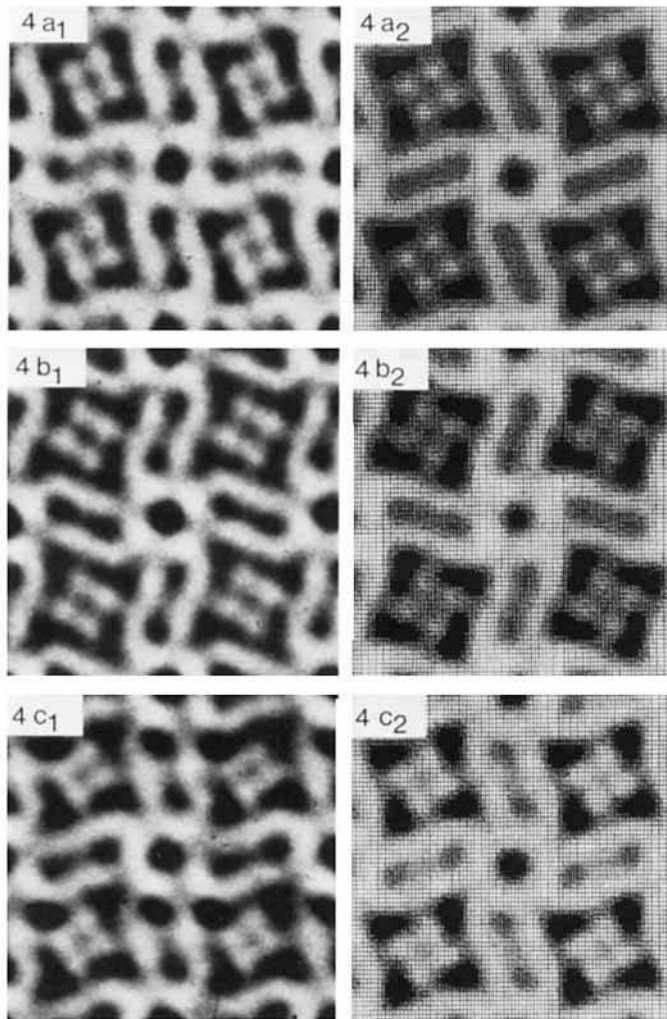
Fig. 4. Symmetrized reconstructions of T–layer cylinder. (a) Upper layer from area "A." (b) Lower layer from area "A." (c) Single layer from area "B." (1) Left-hand side: optical, (2) right-hand side: computer.

Although the optical and computer reconstructions of the different regions of the micrograph shown in Fig. 3a have the same general structure, there are differences in their detailed structure as can be seen from the projection plots* of the optical density of the T-layers. These are presented in Fig. 7a, b. The data used to produce these plots are exactly the same as are used in Fig. 4a2 and 4c2. The arrows point out a small difference between the relative mass-thicknesses of the two reconstructions. This can possibly be ascribed to a greater flattening of the single layer region of the specimen.

*A projection plot has nothing to do with a three-dimensional view of the structure; the z–axis represents the optical density of the reconstruction which is in a first approximation linearly related to the integrated mass distribution (mass thickness) along this direction. These plots should not be interpreted as a surface relief of the layers.
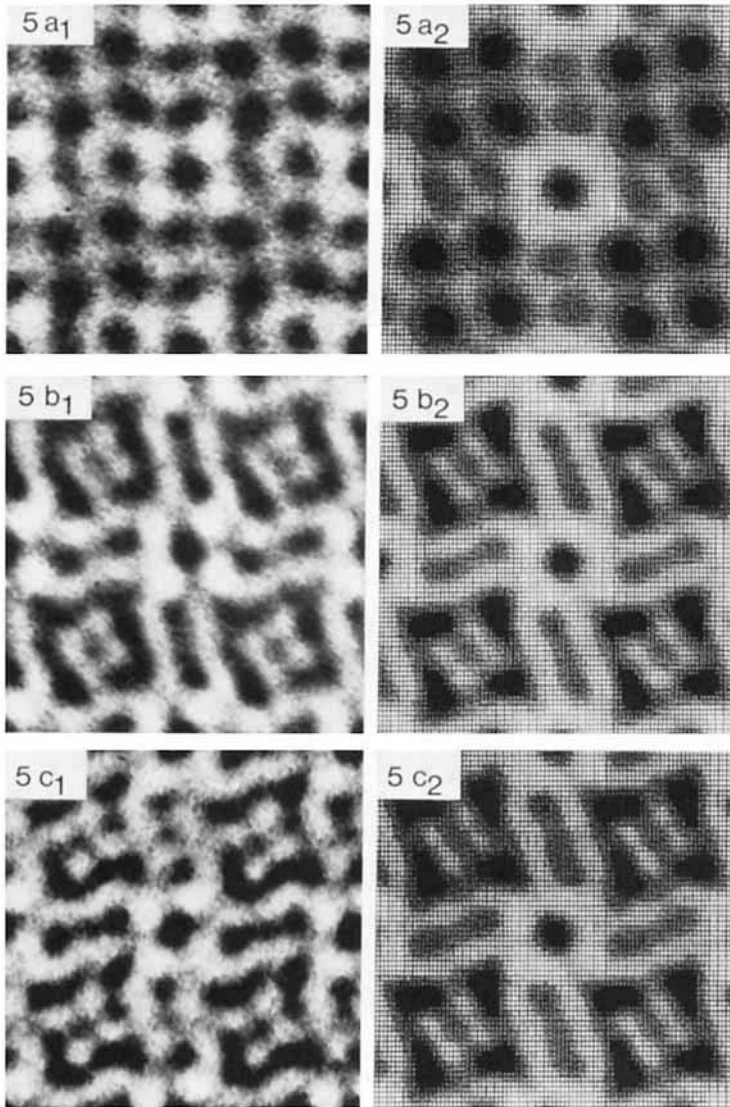
Fig. 5. Unsymmetrized reconstructions of T—layer cylinder of upper layer in Fig. 2a using an increasing number of diffraction orders. (a) 3 orders, (b) 4 orders, (c) 5 orders; (1) left-hand side: optical; (2) right-hand side: computer.

Reconstruction of the Planar Preparations Using 3 and 4 On--Axis Diffraction Orders and a Comparison with the Corresponding Reconstructions of the Cylindrical Form

Micrographs of the planar form prepared in the same way as the cylinders never showed more than 4 on—axis orders in the diffraction patterns (we checked about 50 micrographs). Furthermore, the general appearance of the micrographs seemed to confirm a general lack of fine details. Figure 8a shows a typical micrograph of a planar preparation.

The area used for reconstruction is marked with "A" and its optical diffraction pattern is Fig. 8b. Third- and fourth-order reconstructions are presented in Fig. 9a and b, column 1. In column 2 the corresponding reconstructions of the cylindrical form are shown for comparison. It can be seen that the reconstructions are very similar for both forms; in the cylindrical case, however, the "contours" are much sharper, especially the one of the double arms and of the "minor" tetramer (i.e., the pairs of 4 "globules" which are surrounded by the double arms). The same small differences are visible in the projection plots of 4-order reconstructions of both forms processed under identical conditions; these are shown in Fig. 7a, b, and c.
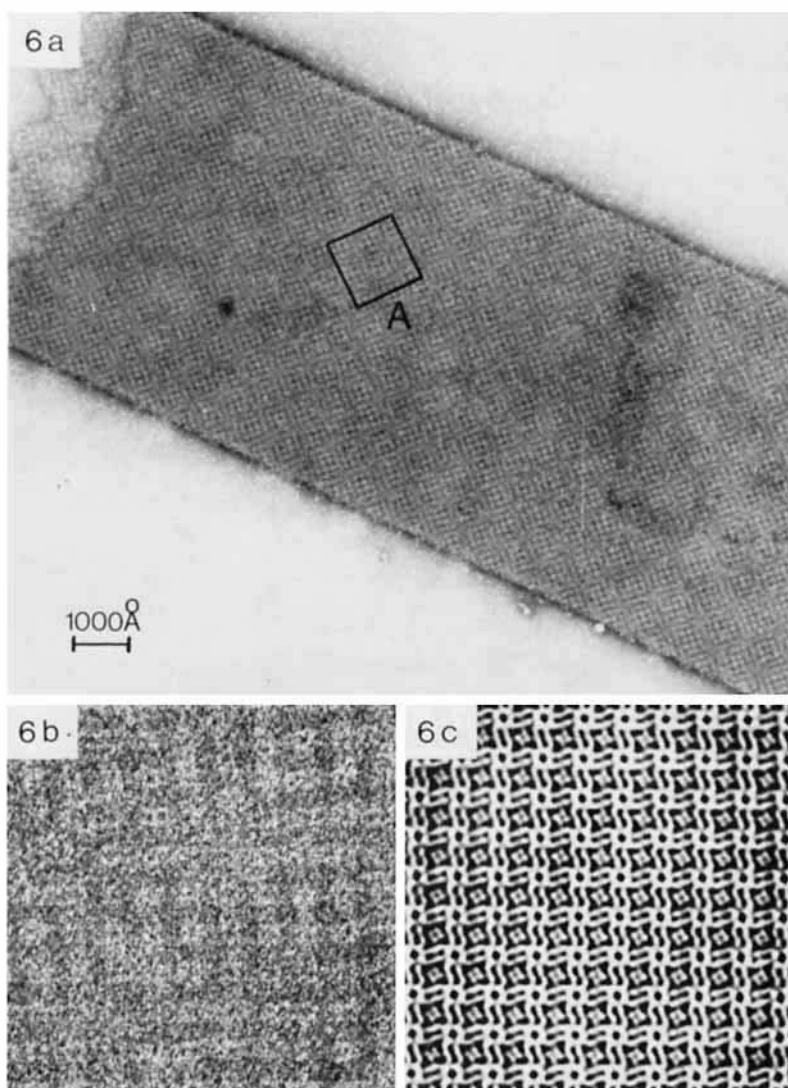
Fig. 6. (a) Micrograph of T–layer cylinder. (b) Enlargement of area "A" (10 × 10 unit cells). (c) Optical reconstruction of the upper layer of area "A"; same magnification as in (b).

As was shown above (Table I and Fig. 2c), the mean lattice constant g is not significantly different between the cylindrical and planar layers. However, in order to establish that the small differences in the reconstructions are significant and not arbitrary we did several controls: all samples which were used for processing were treated under the same conditions (stain, microscopic, and photographic processes). In order to exclude the possibility that the apparently higher information content in the cylindrical samples was not due to its double layer structure, we did two checks: first we processed single layer parts of cylinders (see Fig. 3a, area B and the reconstructions in Fig. 4c and 7b) and, second, we processed double layer parts of planar forms (see Fig. 8a, area B) by filtering away one of the two randomly superimposed plane layers; the results were essentially identical to our previous findings.

Some Considerations Concerning the Curvature of the Cylinders

It is clear from the work of Henry (2) that the planar and cylindrical forms of the T-layer are self-assembly systems, at least *in vitro.* In such systems we expect the
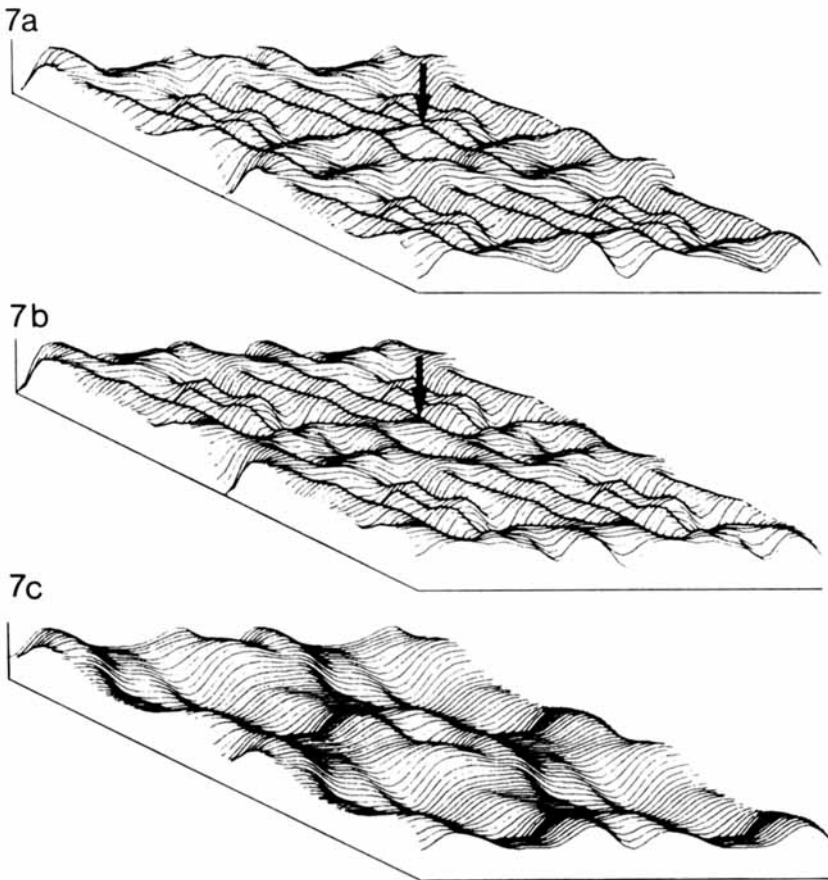

Fig. 7. Projection plot of reconstructions. (a) Data from Fig. $4a_2$. (b) Data from Fig. $4c_2$. (c) Data from Fig. 8a (reconstruction). These should not be interpreted as a surface relief of the layers.

morphology and bonding properties of the protomer to completely define the shape of the assembled structure. In our case it is interesting to calculate an order of magnitude for the distortion of the protomer in a planar T-layer lattice when this lattice is bent into a cylinder. (This is the same distortion one would expect when a cylinder was flattened on the microscope grid.) This distortion might then give a hint as to how the orientations of the bonding areas on the planar T-layer protomers are altered by the pronase action and the extent to which the interprotomer positions and interactions depart from strict equivalence. (Protomers in a cylindrical P4 net must occupy only quasi-equivalent positions.)

   In order to do this calculation we measured the flattened widths of 50 negatively stained cylinders and obtained 7,920 ± 120 Å. Assuming that these were completely
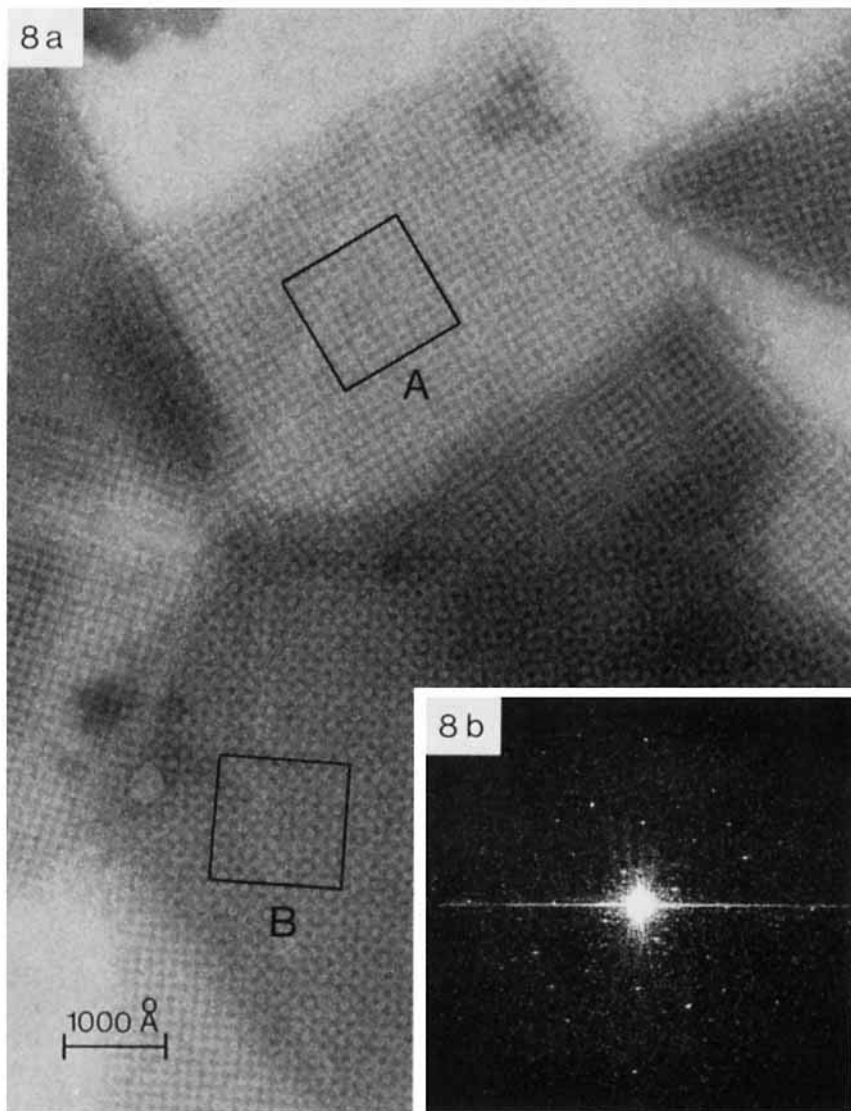

Fig. 8. (a) Micrograph of planar T—layer. (b) Optical diffraction pattern area "A" on Fig. 8a.

flattened (as clearly indicated by the stain distribution) this leads to a value of 2521 ± 38 Å for the cylinder radius. Now the length of the radii of curvature along each of the lattice vectors $\mathbf{g}_1$ and $\mathbf{g}_2$ can be obtained using the formula (18)

$$\rho = R/\cos^2 p$$

where p is the pitch angle of the lattice line considered. From this we get

$$\rho_1 = 4200 \text{ Å along } \mathbf{g}_1$$

and

$$\rho_2 = 6600 \text{ Å along } \mathbf{g}_2$$

From this we can calculate that in order to bend a plane layer into a cylinder each sub-unit must be deflected out-of-plane by distances of

$$S_1 = 2.1 \text{ Å}$$

and

$$S_2 = 1.3 \text{ Å}$$

with respect to its neighbors along the $\mathbf{g}_1$ and $\mathbf{g}_2$ lattice lines, respectively.

If we assume that the protein layer has a thickness of 50 Å (a figure which could easily be wrong by a factor of 2) the difference in linear extent between the top and the bottom of the unit cell in the cylinder would be

$$\delta g_1 = 1.5 \text{ Å}$$

and

$$\delta g_2 = 1.0 \text{ Å}$$

along lattice lines parallel to $\mathbf{g}_1$ and $\mathbf{g}_2$ respectively.

These results clearly show that the T-layer protomers occupy quasi-equivalent positions in the cylindrical P4 lattice because each of the four are distorted in a different way. The distortions themselves are very small, less than 2% of the lattice constant, and, for comparison, an order of magnitude smaller than the corresponding deformations in the case of the P6 surface crystal of T4 polyheads (19). In fact they are so small that they are well below the theoretical resolution limit of our Philips EM 301 microscope.

DISCUSSION AND CONCLUSIONS

Interpretation of the Structurally Significant Results

The statistical analysis and the check for fourfold symmetry have clearly shown that both the planar and cylindrical T-layer lattices are tetragonal with P4 symmetry (calculated deviations from fourfold symmetry < 5% for both forms). The lattice parameters (lattice constants and angle between lattice vectors) of the two forms are identical to better than 1%.

For both forms of T-layer, SDS gel electrophoresis demonstrated that only one protein is involved (2). The amount of the one or two very faint high molecular weight bands (100,000 daltons) which are always present preclude their being part of the protomer.*

*Further work on the electron microscope in dark field has indicated that the T–layer sheets may have a double layer structure, the second layer being very thin and having a much finer structure than the one studied in this paper. Work is continuing to definitively confirm the existence of this second layer and to elucidate its relationship with the coarser T-layer structure.

From the reconstructed distribution of the negative stain (see reconstructions) we have then to conclude that this protein has a very complex mass distribution. In Fig. 10a we show a two-dimensional drawing which can be extracted from the reconstructions compared with a typical optical reconstruction picture, Fig. 10b. It should be noted that our reconstructions do not allow us to decide about the precise manner of dividing the tetramer into four identical parts so as to get the outline of a single protomer. Figure 10a shows one possible division by way of an example; but from the point of view of our data it is entirely arbitrary.

From the reconstruction we have to conclude that despite the different molecular weights of the two forms (140,000 ± 5000 daltons for the planar and 125,000 ± 5000 daltons for the cylindrical form) the general characteristics of their patterns are very similar (see Fig. 9). However, when we compare the projection plots (see Fig. 7) or the digital outputs of the optical density of reconstructed pictures of the two forms we can clearly see that there are significant differences in the relative mass thicknesses of the different parts. In the planar case the contrast between part A and part B (for nomenclature see Fig. 10) is definitely larger than the corresponding one in the cylindrical case. This is also visible in the optical reconstructions shown in Fig. 9b. The same is valid for the contrast between part B and part C. If we exclude the possibility of an unknown
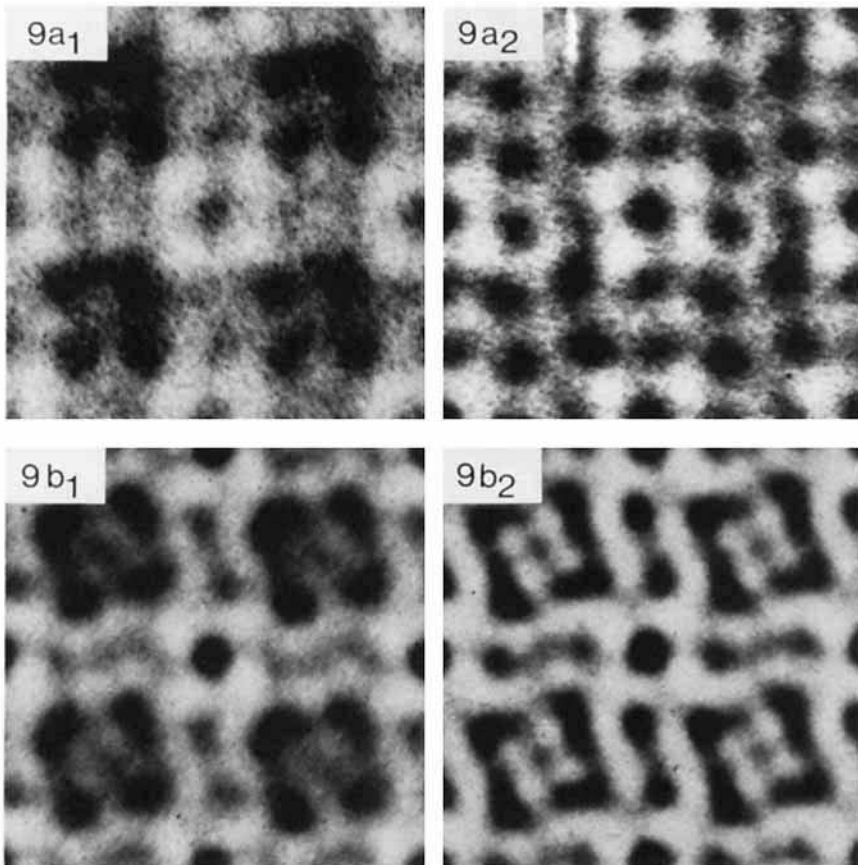

Fig. 9. Comparison of 3- and 4-order reconstructions of planar and cylindrical forms of T–layer. (a) 3 orders, (b) 4 orders. (1) Planar; (2) Cylindrical.

specific staining artifact this would mean that the pronase digests some matter from parts
A and B in the direction perpendicular to the lattice plane. This would lead to a relative
enhancement of the "grooves" along the double arm axes of the tetramer in the cylindri-
cal preparations and provide a simple explanation of the structural differences we actually
observe. This is interesting as the pronase treatment does not significantly alter the
lattice parameters.

In the Results section (Fig. 5) we have studied the build-up of information using
successively 3, 4, and 5 on-axis orders for the reconstructions of the cylindrical form.
From this it becomes clear that all significant periodic information is already included
in the 4-order reconstructions and that the inclusion of the fifth order contributes only
toward minor differences, the significance of which is not obvious. So we have to con-
clude that the structurally significant information that can be extracted from the micro-
graphs reaches approximately 25 Å (including the off-axis orders using a 4 on-axis order
square filter). Roughly the same is true for the planar form except that in this case the
limit seems to be at 30 Å.*

*Measurements of the autocorrelation diameters of the nonperiodic noise in the pictures of the
cylindrical and planar layers gave values of roughly 25 and 30 Å, respectively. It is tempting, therefore,
to use the width at half height of the autocorrelation function of the noise as a measure of the effective
Fourier cutoff of the periodic information. However, no theoretical justification for this is possible
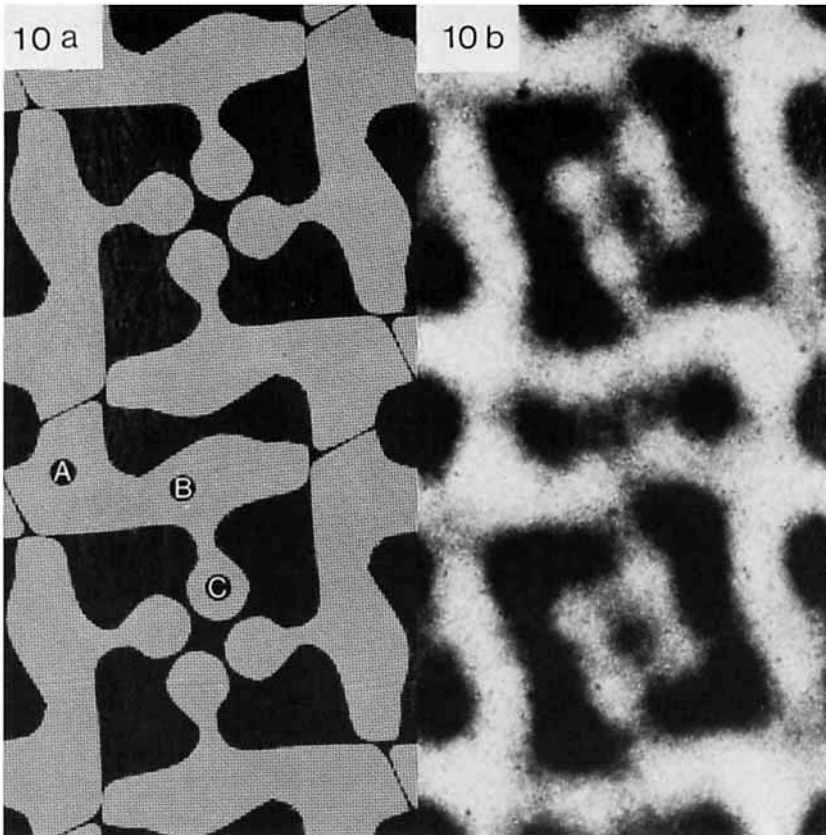independent of a model for the staining process.

Fig. 10. (a) Drawing of T−layer: the division into protomers is arbitrary. (b) Optical reconstruction.

Resolution checks on the microscope resolving power (see Materials and Methods) indicate that the microscope itself was not responsible for the limitation of our significant information to 25 to 30 Å. It seems reasonable therefore to conclude that these limitations arise within the specimen. The structure and distribution of the negative stain, the destruction and degradation of the biological material and the stain by the electron beam, and statistical and systematic deformations of the biological material during preparation limit the amount of information which can be obtained about the specimen from an electron micrograph.

From this we conclude that micrographs of conventionally negatively stained biological specimens do not seem to support a model for the staining process which pictures the stain distribution as possibly damaged but intrinsically smooth down to a few angstroms. Rather it seems that the stain is discontinuous below the 25 Å level and, in all but a few special cases, unable to provide contrast to structures smaller than this. Clearly, a great deal of work is needed to study the staining process and the relation between specimen structure and contrast.

Comparison Between Optical and Computer Reconstructions

From our reconstructions it became clear that there is little difference between the output of the optical system and that of the computer. It hould be emphasized, however, that the computer output we have used for this study (line printer output) has obvious drawbacks as it represents the reconstructed gray level scale very poorly compared with the projection plots or digital output. The output possibilities we presently have (apart from the digital output) could not allow us to show and emphasize any greater versatility or accuracy of the computer in comparison with the optical system.

It is important to realize that from a general point of view the aim of the optical and the computer systems is to process information in the micrograph about the structure of the object imaged in the microscope. Systems should be judged as to whether inefficiencies in information transfer, artifacts, and noise are likely to lead to an incorrect interpretation of the processed data as to the structure of the specimen. It is not clear from our work whether or not computer results would be significantly better than the optical results in this respect even with an optimal output system. The flexibility of the computer was, however, a considerable help in solving a number of ancillary problems (such as the search for symmetries, correction of lattice distortions, etc.) and fully justified its use from this point of view.

It is clear from the work of Amos and Klug (11) and Finch (20) that the precision and flexibility of computer processing is essential in some particularly difficult situations. Our work does show, however, that careful and systematic use of an optical diffractometer can provide reconstructions of high quality which are not likely to be improved by computer reconstruction in most cases.

APPENDIX
P. R. Smith and U. Aebi

INTRODUCTION

The purpose of this appendix is to discuss in more detail some of the analyses in this paper. Most of these are mathematical and would therefore be out of place in the body of the work, but they are important for a clear understanding of the methods. Most of them in addition have not been published, at least not in a biologically oriented journal.

The appendix is in two parts: the first part discusses the Fourier transform filtering problem, shows how averaging is done in the optical and computer cases, and points out in detail how the two operations differ. The second part presents a discussion of the bilinear interpolation used extensively in our analysis.

FILTERING CONTINUOUS AND DISCRETE FOURIER TRANSFORMS

The functional form of the ideal image is as follows:

$$g(x) = h(x) \cdot [l(x) * m(x)]$$

where

$l(x)$ is an infinite periodic array of delta functions; $m(x)$ is a function which describes the motif, zero outside the unit cell of $l(x)$; $h(x)$ is a function which defines the overall size of the structure, in our case, a square or a circular area enclosing several periods of $l(x)$; and the asterisk (*) denotes the convolution operation, a description of which can be found in Goodman (22) together with the convolution theorem of which we will make extensive use of below.

The Fourier transform of $g(x)$, $G(k)$, has the following form (a capital letter will be used to denote the Fourier transform of the real space function written with a corresponding small letter):

$$\text{F.T.: } g(x) \longrightarrow G(k)$$

$$G(k) = H(k) * [L(k) \cdot M(k)]$$

where $L(k)$ is an infinite array of delta functions identical to the reciprocal lattice of $l(x)$; $M(k)$ is the Fourier transform of the motif $m(x)$; and $H(k)$ is the Fourier transform of the window $h(x)$, in our case a double sinc function or an Airy function (22).

The basic form of the transform is an array of delta functions $L(k)$ modulated by the transform of the motif. The convolution operation then replaces each delta function with the transform $H(k)$.

In practical cases $h(x)$ is made as large spatially as possible and $H(k)$ is consequently very narrow. Consequently $G(k)$ is only large in small regions around the lattice points of $L(k)$.

In practice the experimental data $g'(x)$ will not have the ideal form just defined. We can, however, write the measured data as a sum of a noise component $n(x)$ and an ideal (unknown) structure $g(x)$:

$$g'(x) = g(x) + n(x)$$

The aim is, therefore, to have a filtering procedure which transmits an optimal amount of information about g $(\mathbf{x})$ and eliminates as much as possible of the noise n $(\mathbf{x})$.

The transform of n $(\mathbf{x})$, N $(\mathbf{k})$, has, in general, a broad spectrum of spatial frequencies whereas G $(\mathbf{k})$ has its contributions concentrated around the lattice points of L $(\mathbf{k})$. Consequently, if we construct a simple filter, S $(\mathbf{k})$, such that

$$S(\mathbf{k}) = \begin{array}{l} 1, |G(\mathbf{k})| \gg |N(\mathbf{k})| \\ 0, \text{elsewhere,} \end{array}$$

we will transmit information about g $(\mathbf{x})$ in preference to that about n $(\mathbf{x})$. The operation can be summarized as follows.

Filtering Procedure

$$g'(\mathbf{x}) = g(\mathbf{x}) + n(\mathbf{x})$$

Fourier transform: $\quad g'(\mathbf{x}) \longrightarrow G'(\mathbf{k}) = G(\mathbf{k}) + N(\mathbf{k})$

Filtering: $\quad G'(\mathbf{k}) \longrightarrow G'_F(\mathbf{k}) = S(\mathbf{k}) \cdot G'(\mathbf{k})$

Fourier transform^{-1}: $\quad G'_F(\mathbf{k}) \longrightarrow g'_F(\mathbf{x}) = s(\mathbf{x}) * g'(\mathbf{x})$

$$= s(\mathbf{x}) * g(\mathbf{x}) + s(\mathbf{x}) * n(\mathbf{x})$$

(See also reference 21.)

In the optical realization of the filtering operation S $(\mathbf{k})$ has a fixed form, usually

$$S(\mathbf{k}) = B(\mathbf{k}) \cdot [W(\mathbf{k}) * L(\mathbf{k})]$$

where L $(\mathbf{k})$ is the reciprocal lattice of l $(\mathbf{x})$ and is an infinite array; W $(\mathbf{k})$ is the filter hole function (a square or a circle); and B $(\mathbf{k})$ is the band limiting function and is identical to the overall shape of the filter. Because the Fourier transforms with which we deal are essentially zero outside a region which is still inside our filter, we will take B $(\mathbf{k})$ to be equal to 1 for all $\mathbf{k}$; this is usually a good approximation. With this approximation S $(\mathbf{k})$ can be written as follows: S $(\mathbf{k})$ = W $(\mathbf{k})$ * L $(\mathbf{k})$. It's Fourier transform, s$(\mathbf{x})$ = w $(\mathbf{x})$ · l $(\mathbf{x})$, is therefore an infinite periodic array of delta functions which are weighted by w $(\mathbf{x})$. Consequently

$$g'_F(\mathbf{x}) = [w(\mathbf{x}) \cdot l(\mathbf{x})] * g'(\mathbf{x})$$

is built up by superposing the image g$'$ $(\mathbf{x})$ onto itself, each subsequent contribution being weighted by the factor w $(\mathbf{x}_i)$ where $\mathbf{x}_i$ is a vector to one of the lattice points l $(\mathbf{x})$. This operation is equivalent to a Markham superposition but with weights different from l. The extent of the effective averaging is governed by the spatial extent of W $(\mathbf{k})$; the smaller it is the larger the region of w $(\mathbf{x})$ where it is effectively 1; for very large $\mathbf{x}$, w $(\mathbf{x})$ = 0.

In the limiting case where W $(\mathbf{k})$ = δ $(\mathbf{k})$, w $(\mathbf{x})$ = 1 everywhere and the filtering is identical to the Markham superposition operation.

As a result of the filtering we may write

$$g'_F(\mathbf{x}) = g_F(\mathbf{x}) + n_F(\mathbf{x})$$

where

$$g_F(\mathbf{x}) = s(\mathbf{x}) * g(\mathbf{x})$$

$$n_F(\mathbf{x}) = s(\mathbf{x}) * n(\mathbf{x})$$

g$_F$ $(\mathbf{x})$ is now a function of the form

$$g_F(\mathbf{x}) = \int v(\mathbf{x}, \mathbf{u}) \cdot m(\mathbf{u}) \cdot d\mathbf{u}$$

where in general

$$v(\mathbf{x}, \mathbf{u}) = \sum_{p,q}^{\infty} \delta(p\vec{\alpha}_1 + q\vec{\alpha}_2 + \mathbf{u} - \mathbf{x}).$$

$$\left[\sum_{m,n}^{\infty} w([p+m]\vec{\alpha}_1 + [q+n]\vec{\alpha}_2 + \mathbf{u} - \mathbf{x}) \cdot h(\mathbf{u} + m\vec{\alpha}_1 + n\vec{\alpha}_2) \right] \qquad (\mathbf{u} + m\vec{\alpha}_1 + n\vec{\alpha}_2)]$$

with $\vec{\alpha}_1 \ \vec{\alpha}_2$ are the lattice vectors of l $(\mathbf{x})$ and p, q, m, and n are integers. In our case this simplifies to give

$$v(\mathbf{x}, \mathbf{u}) = v(\mathbf{x} - \mathbf{u}) = \sum_{P,q}^{\infty} \delta(p\vec{\alpha}_1 + q\vec{\alpha}_2 + \mathbf{u} - \mathbf{x}) \cdot \sum_{m,n}^{N'} w([p+m]\vec{\alpha}_1 + [q+n]\vec{\alpha}_2 + \mathbf{u} - \mathbf{x})$$

where N' is one less than the multiple of the lattice constant which is equal to the length of the side of the square, h $(\mathbf{x})$. With this simplification the integral defining $g_F(\mathbf{x})$ is clearly a convolution integral.

$n_F(\mathbf{x})$ is still a "noise" function but its power is considerably reduced because all nonperiodic contributions to it have been eliminated. Periodic noise or noise correlated with the structure (e.g., the systematic collapse of some regions due to the stain) will not be removed by this filter.

Computer filtration differs from the optical analogue transform principally in that the transform is discrete. In fact what is calculated is the transform of the function

$$g_p'(\mathbf{x}) = q(\mathbf{x}) \circ [y(\mathbf{x}) * g'(\mathbf{x})]$$

where q$(\mathbf{x})$ is an infinite array of delta functions which constitutes the sampling grid of the function we wish to transform, (if one is using some computer system only a finite amount of data can be processed and so some sampling is necessary), and y $(\mathbf{x})$ is an infinite array of delta functions whose periodicity is given by the width of the nonzero region of g' $(\mathbf{x})$. The periodicity of q is chosen so that a transform of the function above is simply

$$Q(\mathbf{k}) * [Y(\mathbf{k}) \circ G'(\mathbf{k})]$$

The factor Y $(\mathbf{k})$ is the Fourier space sampling raster and it comes from the periodic continuation of the real space function.

G' $(\mathbf{k})$ is the original function which we wished to study but now we have an additional convolution with Q $(\mathbf{k})$, an array of delta functions coming from the sampling grid. This has the effect of mixing frequencies separated by multiples of the lattice constant of Q $(\mathbf{k})$, a process called aliasing (23). As the real space sampling raster gets finer the mixing takes place over longer distances in Fourier space and in general is taken to be negligible when the real space sampling distance is less than $1/3-1/4$ of the wavelength of the highest significant spatial frequency (23).

The important difference between the continuous and discrete transforms is, therefore, that the discrete transform values are contaminated by aliasing errors.

In order to avoid artifacts arising from aliasing errors and to optimize the signal-to-noise ratio in our computer filtering, we chose the window size, h, and the sampling distances so that an integral number of periods of l $(\mathbf{x})$ lay inside the window, and the lattice constant of l $(\mathbf{x})$ was chosen to be an integral multiple of the lattice constant of q $(\mathbf{x})$. With this choice, the spatial frequencies needed for the reconstruction fall exactly on Fourier space sample points and consequently contribute to one and only one sample

point. The "mask" then selects just these transform points, and the inversion formula simply calculates averages of the periodically related real space points. This averaging process is just the computer equivalent of the Markham superposition. Aliasing still occurs, of course but the effect of it is to alias periodically related frequencies with each other. Nonperiodic information does not contribute to these frequencies and so no artefacts of this type can arise.

To summarize briefly: provided we are careful to choose a sampling raster and window size according to the rules given above, the analogue and computer filtering operations differ only in the effective hole size of the filter. In the computer case the hole size is effectively zero and the filtering is equivalent to a Markham superposition. In the analogue case the hole size is finite and the filtering is then equivalent to a Markham superposition but with different weights for each unit cell averaged.

THE BILINEAR INTERPOLATION SCHEME

In the solution of computational problems it is often necessary to have an estimate of a measurable quantity at a point at which no measurement has been made. In these cases an interpolation scheme is usually used to provide an estimate of the quantity at this new point. Generally speaking there are three criteria which are applied when chosing an interpolation scheme: 1. The interpolation scheme should be based on a model for the variation of the measured data in the absence of noise. 2. Given a particular (appropriate) interpolation scheme and interpolation geometry, noise in the measurements should not be amplified when the estimates are calculated. 3. The correlation radius of the possible noise contributions should remain unaltered or at least changes in it should not alter the results.

Unfortunately, in our case no precise mathematical model can be constructed for the raw data produced by the densitometer and so we have no way to satisfy the first of these conditions. In spite of this we do expect a smooth variation in data collected at points separated by a small distance in relation to the smallest significant resolution distance we expect to see on a micrograph. Furthermore, the purpose of our interpolation was to alter the positions of sample points rather than their number. Consequently pre-
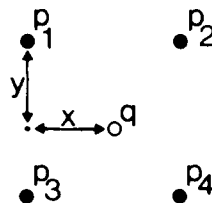
$$q = y(xp_1 + (1-x)p_2) + (1-y)(xp_3 + (1-x)p_4)$$

x : fraction of distance between x
        sample points
y : fraction of distance between y
        sample points

Fig. A1. The bilinear interpolation scheme.
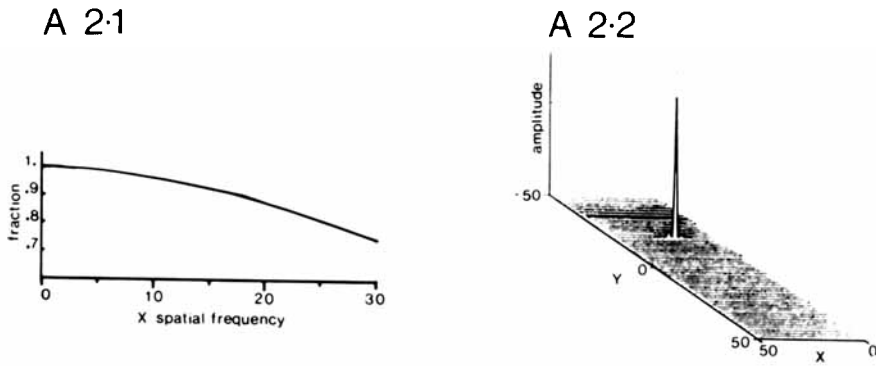
A 2·1

A 2·2

Fig. A2. (1) Fraction of the amplitude of a diffraction spot in x direction transmitted by the bilinear interpolation. (2) Spreading of the amplitude of a diffraction spot due to the bilinear interpolation.
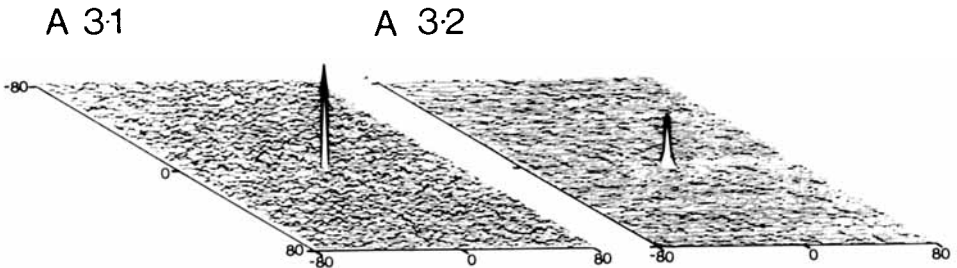
A 3·1   A 3·2

Fig. A3. Autocorrelation functions (1) of computer generated random numbers, (2) of interpolated computer generated random numbers.

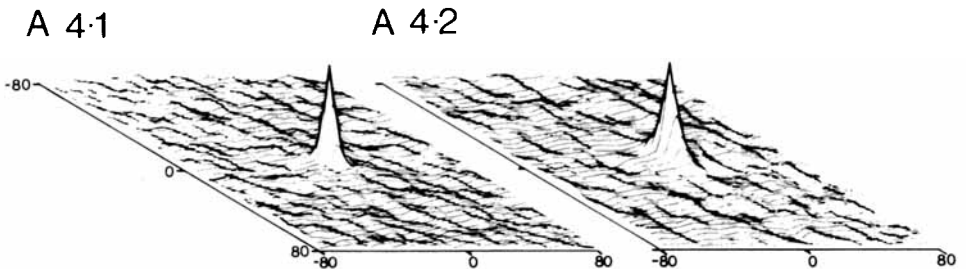A 4·1   A 4·2

Fig. A4. Autocorrelation functions (1) of noise from the single layer in Fig. 3aB. (2) Of noise from the planar layer in Fig. 8aA.

cautions to preserve the continuity of derivatives at the measured points were unnecessary and a bilinear interpolation scheme (see Fig. A1) was chosen for its simplicity and speed.

As the data we used was eventually resolved into its Fourier components a test of the information transferring capability of the interpolation scheme was to lineraly interpolate ideal data for various spatial frequencies from a skew system into a square system and to see how this was degraded. Results are given in Fig. A2.1, where we have graphed the fraction of the amplitude of various spatial frequencies transmitted by this interpolation

scheme, and in Fig. A2.2 where we show how one spatial frequency's amplitude was spread into other spatial frequencies. These results depend upon the geometry of the skew system of course. In our case we looked at 100×100 arrays with the Y axis skewed by an angle of $+1.18°$ from $90°$. Such results indicate that when the errors due to the spreading of the spatial frequencies are likely to be small an amplitude transmission filter can be constructed to compensate for the power loss in the high-frequency terms. Such a filter is expensive to construct and we did not feel that its use would be justified in our case.

The second point to be checked is that noise is not amplified by interpolation. This was done by interpolating random noise and inspecting the result using the same geometry as used above. The result was an apparent reduction in the RMS value of the noise by a factor of roughly 0.7. This is to be expected as clearly the interpolated value, i, must be smaller than the largest value, d_{max}, in the surrounding square (see Fig. A1); that is,

$$d_{max} \geqslant i \geqslant d_{min}$$

The last point concerning the correlation radius of the noise was tested using computer-generated random numbers once again. Autocorrelation functions of the noise and the interpolated noise can be seen in Fig. A3.1 and A3.2. It is clear that the effect of the interpolation has been to increase the correlation radius of the noise. From the equation given in Fig. A1 it is clear that the maximum increase in the correlation radius is 1 unit, and this is the result we do in fact obtain. For comparison (Fig. A4.1 and A4.2) we include autocorrelations of the noise obtained from the cylinder and planar pictures (Fig. 3a and 8a). In this case "noise" was defined as anything not falling inside the filter holes. An increase in either of these two correlation radii by 1 unit is unlikely to seriously distort the results.

ACKNOWLEDGMENTS

REFERENCES

1. McNary, J. E., Brinton, C. C., and Carnahan, J., Bact. Proc., SP30 (1969).
2. Henry, C. M., Ph.D. Thesis, Dissertation Abstracts, International, 33:73−2878, p. 4409−B (1972).
3. Klug, A., and Berger, L. E., J. Mol. Biol. 10:565−569 (1964).
4. Klug, A., and De Rosier, D. J., Nature 212:29−32 (1966).
5. Moody, M. F., Phil. Trans. Roy. Soc. Lond. B261:181 (1971).
6. De Rosier, D. J., and Klug, A., J. Mol. Biol. 65:469−488 (1972).
7. Yanagida, M., De Rosier, D. J. and Klug, A., J. Mol. Biol. 65:489−499 (1972).
8. Leonard, K. R., Kleinschmidt, A. K., Agabian-Keshishian, N. et al., J. Mol. Biol. 71:201−216 (1972).
9. Finch, J. T., Klug, A., and Nermut, M. V., J. Cell Sci. 2:587−590 (1967).
10. Cochran, W. T., Cooly, J. W., Favin, D. L. et al., IEEE Trans.: Au−15 (2), 45 (1967).
11. Amos, L. A., and Klug, A., Proc. Fifth European Congress Electron Microscopy, 580−581 (1972).
12. De Rosier, D. J., and Klug, A., Nature 217:130−134 (1968).
13. Crowther, R. A., Phil. Trans. Roy. Soc. Lond. B261:221−230 (1971).
14. Markham, R., Frey, S., and Hills, G. J., Virology 20:88−102 (1963).
15. Valentine, R. C., Advances in Optical and Electron Microscopy 1:180, Academic Press, (1966).
16. Williams, R. C., and Fisher, H. W., J. Mol. Biol. 52:121−123 (1970).
17. MacLeod, I. D. G., IEEE Trans.: Au−19, 160−162 (1970).
18. King, M. V., and Young, M., J. Mol. Biol. 65:519−523 (1972).
19. Scraba, D. G., Raska, I., Kellenberger, E., and Moor, H., J. Ultrastructure Res. 44:27−40 (1973).
20. Finch, J. T., (1972) private communication.
21. Fraser, R. D. B., and Millward, G. R., J. Ultrastructure Res. 31:203−211 (1970).
22. Goodman, J. W., "Introduction to Fourier Optics," McGraw-Hill, New York, (1968).
23. Bracewell, R., "The Fourier Transform and Its Applications," McGraw-Hill, New York (1965).